EES Batteries

PAPER

View Article Online
View Journal

Cite this: DOI: 10.1039/d5eb00166h

An internal–external dual-modification strategy for enhancing interfacial stability and ionic transport in LATP-based solid-state electrolytes

Mou Yang,[a] Qing Liu,*[b] Kun Zeng,[a] Genfu Zhao,[a] Li Yang,[a] Qingxia Hu,[a] Xilin Liang,[a] Shuyuan Yu[a] and Hong Guo *[a]

Received 9th September 2025,
Accepted 30th October 2025

DOI: 10.1039/d5eb00166h

rsc.li/EESBatteries

NASICON-type $Li_{1.3}Al_{0.3}Ti_{1.7}(PO_4)_3$ (LATP) is a potential solid electrolyte, favored for its high ionic conductivity, excellent air stability and low cost. However, direct contact between LATP and lithium induces Ti^{4+} reduction to Ti^{3+}, causing mechanical stress and structural degradation at both the interface and within the LATP structure, which severely limits solid-state battery applications. Here, we propose a novel internal–external dual-modification strategy to simultaneously optimize the bulk structure and interfacial stability of LATP-based solid-state electrolytes. Internally, ultra-fast Joule heating sintering densifies LATP, reduces grain boundary resistance, and enhances lithium-ion transport. Externally, an *in situ* crosslinked polyethylene glycol diacrylate-based gel polymer electrolyte (PGPE) serves as an interfacial buffer layer, providing ionic conductivity, electronic insulation, and stress buffering. This hierarchical design enables the formation of a PGPE@P-LATP-J composite electrolyte which exhibits a wide electrochemical window (4.91 V), high ionic conductivity (1.14×10^{-3} S cm^{-1}), and a lithium-ion transference number of 0.79. The modified LATP-based solid-state $LiFePO_4$ (LFP) cells achieved 99.1% capacity retention after 200 cycles at 1C, and the Li/Li symmetric cells maintain stable cycling over 1500 hours at 0.5 mA cm^{-2}. This work offers a practical strategy to address interfacial degradation in LATP-based systems and promotes the development of high-performance solid-state lithium batteries.

Broader context

Solid-state electrolytes (SSEs), with inherent non-flammability and high stability, are regarded as promising candidates for liquid electrolytes. Among them, $Li_{1.3}Al_{0.3}Ti_{1.7}(PO_4)_3$ (LATP), as a NASICON structure solid electrolyte, is regarded as one of the ideal materials for all-solid-state batteries due to its excellent air stability, high ionic conductivity, and cost-effectiveness. However, the high interfacial impedance between LATP and the electrode, as well as the severe interfacial side reactions with metallic lithium, has greatly restricted its practical application. Therefore, developing LATP-based electrolytes with stable interfaces and low grain boundary resistances is a necessary condition for meeting future energy storage demands. Herein, a novel internal–external dual-modification strategy is employed to systematically optimize the structure and interfacial properties of LATP-based SSEs. This unique system successfully enhanced the Li^+ conductivity, mechanical strength and high-pressure resistance of LATP-based SSEs. This study provides a feasible and scalable pathway to overcome the intrinsic interface challenges of LATP-based electrolyte systems and offers valuable guidance for the design of high-performance solid-state lithium batteries.

1. Introduction

Conventional graphite anode with liquid electrolytes has nearly reached its capacity limit, restricting further battery performance enhancements.[1] Lithium metal anodes, with a theoretical capacity of 3860 mAh g^{-1} and the lowest potential of −3.04 V (*versus* standard hydrogen electrodes), have become the preferred choice to break through the energy density bottleneck.[2–4] However, continuous interfacial side reactions with liquid electrolytes and the flammability of low-boiling-point solvents result in poor cycling stability and high risk of thermal runaway.[5–7] Solid-state electrolytes, with inherent non-flammability and high stability, are regarded as promising candidates for liquid electrolytes.[8,9] Among them, NASICON-type $Li_{1.3}Al_{0.3}Ti_{1.7}(PO_4)_3$ (LATP) has attracted significant attention owing to its excellent air stability, high ionic conductivity, and cost-effectiveness.[10,11] Nevertheless, direct contact between LATP and lithium induces the reduction of Ti^{4+} to Ti^{3+}, leading to mechanical stress and structural degradation at the

[a]School of Materials and Energy, Yunnan University, Kunming 650091, China. E-mail: guohong@ynu.edu.cn
[b]Faculty of Chemical Engineering, Kunming University of Science and Technology, Kunming 650500, P. R. China. E-mail: liuqing_a0510@163.com

interface.[12–14] This degradation increases interfacial resistance, causes uneven lithium deposition, and promotes the formation of inactive lithium, significantly undermining battery performance and safety.[15–17] Moreover, conventional sintering methods for LATP often cause lithium volatilization, grain coarsening, and high grain boundary resistance, limiting its practical application.[18–20] To improve the stability and ion transport efficiency at the lithium metal anode/solid electrolyte interface, various organic and inorganic interfacial modification strategies have been developed, including zinc oxide,[21] zinc fluoride,[22] boron nitride,[23] and polyvinyl[24] ether. Inorganic interlayers provide superior chemical stability and can suppress dendrite growth but typically require high-temperature lithium welding, which involves high energy consumption and safety concerns.[25] Conversely, organic interlayers benefit from mild processing conditions and better interfacial wettability but suffer from relatively low ionic conductivity and poor interfacial adhesion.

In situ polymerization has emerged as a promising approach due to its controllable reaction kinetics, uniform film formation, and gentle processing conditions, effectively enhancing interfacial ion transport.[26–30] Unfortunately, many existing systems rely on polymers with low mechanical strength, which are prone to interfacial failure under operational stress. Polyethylene glycol diacrylate (PEGDA), as a high-performance crosslinker, forms a dense three-dimensional network *via in situ* polymerization, enhancing mechanical integrity and stabilizing ion migration while resisting stress damage.[31–34] Notably, the effectiveness of PEGDA-based gels is inherently linked to the structural quality of the LATP ceramic substrate. The traditional solid-phase synthesis of LATP usually involves methods such as melting quenching[35] and mechanical activation.[36] Normally, in the solid-phase methods, the solid chemical precursors are mixed together and ball milled, followed by solid-state reactions through annealing and sintering treatment. Such processes can induce abnormal grain growth and reduce microstructural uniformity. In addition, prolonged high-temperature treatments tend to cause lithium volatilization, adversely affecting the ionic conductivity and chemical stability of LATP (Fig. 1a). Thus, there is an urgent need to develop mild, controllable intermediate layer and sintering methods that maintain lithium-conducting structures while minimizing lithium loss. Although flexible polymer interlayers have been employed to mitigate side reactions at the lithium–ceramic electrolyte interface, these strategies primarily focus on macroscopic surface coverage and often overlook potential electron leakage and ion transport barriers at the microscopic interfaces between LATP particles. The lack of precise regulation of ion-selective transport and electron blocking within particle-level channels leads to failure modes such as structural cracking, interfacial delamination, and performance degradation under high current densities and extended cycling.[37] Therefore, synergistic integration of the *in situ* crosslinked PEGDA polymer network with porous LATP ceramics, coupled with the development of flexible composite interface layers exhibiting electronic insulation, ionic conductivity, stress buffering, and nanoscale interfacial regulation, represents a critical breakthrough for enhancing interface stability and ensuring the long-term reliability of solid-state electrolytes. Furthermore, the compatibility and structural robustness of PEGDA in conjunction with LATP-based solid electrolytes for composite interface fabrication have been scarcely investigated.

Herein, we propose a novel internal–external dual-modification strategy to systematically optimize the structure and interfacial properties of LATP-based solid-state electrolytes.

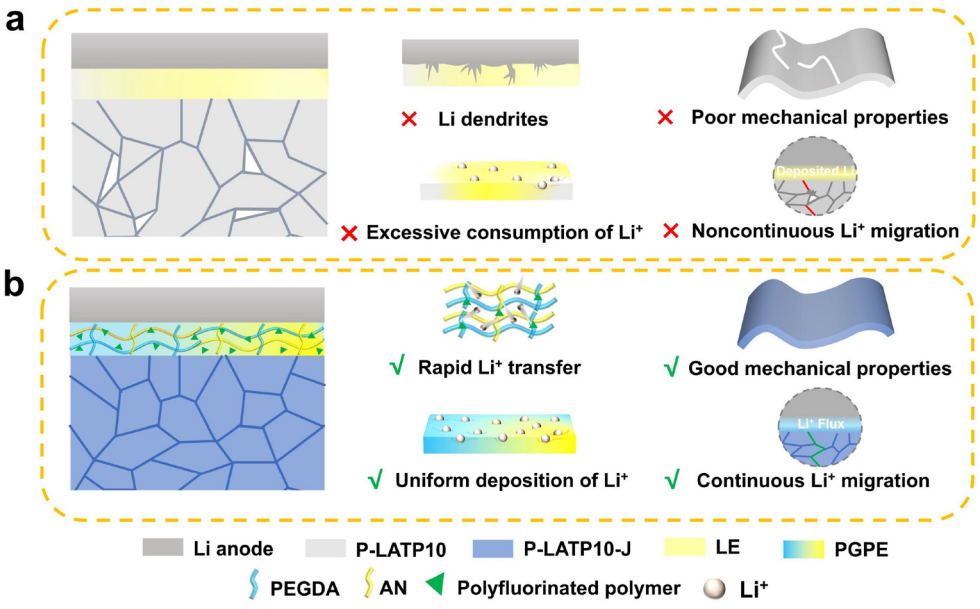

Fig. 1 Schematic illustration of the Li/LATP interface. Comparative analysis of the advantages of (a) P-LATP and (b) PGPE@P-LATP-J.

First, LATP is processed *via* Joule heating ultra-fast high-temperature sintering, which significantly reduces grain boundary impurity aggregation, improves grain size distribution and material density, and blurs grain boundaries. These changes markedly lower grain boundary resistance and enhance lithium-ion migration. Second, the LATP powder is fabricated into an electrolyte membrane using a solution casting method, which effectively improves particle dispersion and enhances the overall mechanical strength and thermal stability of the composite solid-state electrolyte, thus improving the structural safety of the battery system. Third, a PEGDA-based gel polymer electrolyte (PGPE) is designed as an intermediate interface layer. *In situ* polymerization forms a dense cross-linked network with excellent affinity for lithium metal and robust mechanical support. The PGPE layer effectively prevents direct contact between LATP and lithium, reduces interfacial side reaction sites, and promotes uniform lithium-ion deposition and stripping (Fig. 1b). The obtained PGPE@P-LATP-J composite electrolyte, developed through this triple synergistic optimization, exhibits outstanding electrochemical performance with a stable voltage window reaching up to 4.91 V, a lithium-ion transference number of 0.79, and an ionic conductivity of 1.14×10^{-3} S cm^{-1} at room temperature. The modified LATP-based solid-state $LiFePO_4$ (LFP) cells demonstrate excellent cycling stability, retaining 99.1% of their initial capacity after 200 cycles at 1C. The Li/Li symmetric battery achieved a long cycling stability of over 1500 hours at 0.5 mA cm^{-2}. Moreover, various *in situ* measurements further confirmed the positive impact of the internal–external dual-modification strategy on solid-state electrolytes.

2. Results and discussion

Design and characterization of the LATP-J composite electrolyte

To achieve more effective internal modification of LATP electrolytes, Joule-heating rapid sintering was employed as an alternative to conventional solid-state sintering, aiming to enhance the interfacial properties and microstructure of the resulting material. The temperature variation of Joule heating ultrafast sintering is shown in Fig. S1. The temperature of the sample was uniformly distributed during the sintering process to achieve the best sintering result. First, the crystallinity and phase purity of LATP-J were investigated to determine the optimal sintering temperature. As shown in Fig. S2 and Fig. 2a, the XRD patterns of LATP-J powders sintered at different temperatures (1000 °C, 1100 °C, 1200 °C, and 1300 °C) for 15 s were recorded and compared with the standard pattern of cubic $LiTi_2(PO_4)_3$ (PDF#35-0754). The LATP precursor was rapidly heated using a carbon boat as the Joule heating element, allowing precise control of temperature and duration through electrical power input. Among these samples, the LATP-J sintered at 1100 °C showed the best match with the reference pattern, indicating successful phase formation. However, when sintered at lower temperatures,

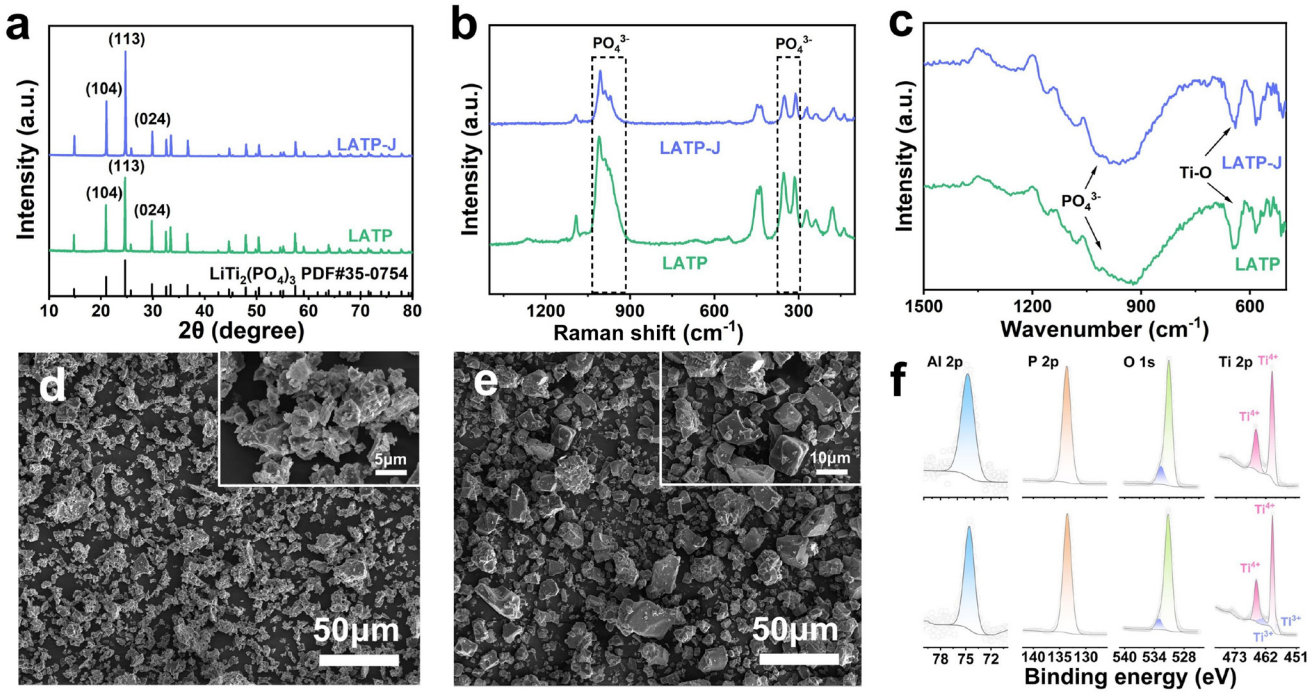

Fig. 2 Characterization of LATP-J. (a) The XRD pattern of LATP-J and LATP. (b) The FT-IR spectra of LATP-J and LATP. (c) The Raman spectra of LATP-J and LATP. (d) The SEM image of the Joule furnace-sintered LATP powder. (e) The SEM image of the solid-state sintered LATP powder. (f) The XPS spectrum of LATP (bottom) and LATP-J (top).

residual peaks from raw materials were observed, such as TiO_2 and Al_2O_3 at 22.4° and 27.4°, respectively. These peaks indicated incomplete solid-state reactions, and that the LATP phase had not been fully developed, resulting in low crystallinity and poor densification. Furthermore, at higher sintering temperatures (1300 °C), impurity diffraction peaks from $LiTiPO_5$ and $AlPO_4$ appeared at 21.5° and 27.7°, suggesting the formation of unwanted phases due to excessive heat, which can also compromise the electrochemical performance. In contrast, impurity phases were observed in LATP-J samples sintered at other temperatures, suggesting that the sintering conditions were not optimal. To further confirm the phase composition, Raman spectroscopy was performed on both LATP and LATP-J samples (Fig. 2b). The characteristic peaks corresponding to the PO_4^{3-} vibrations, observed at 301–373 cm^{-1} and 918–1034 cm^{-1}, were consistent with the typical Raman shifts for $LiTi_2(PO_4)_3$, as reported in previous studies.[38,39] In addition, Fourier transform infrared spectroscopy (FT-IR) analysis (Fig. 2c) revealed broad absorption bands between 1300 and 700 cm^{-1}, associated with the stretching vibrations of the PO_4^{3-} groups. The broad Ti–O stretching vibration observed in the 600–750 cm^{-1} range was also consistent with the literature on similar titanium phosphate materials.[40] These spectroscopic results further confirmed the successful synthesis of LATP and LATP-J. Further comparison of the scanning electron microscopy (SEM) images revealed that LATP-J particles (Fig. 2d), prepared *via* Joule heating, exhibit significantly smaller and more uniform sizes compared to those of LATP synthesized using the conventional sintering method (Fig. 2e). In addition, Brunauer–Emmett–Teller (BET) analysis showed that the specific surface area of LATP-J increased from 1.339 $m^2\ g^{-1}$ to 2.718 $m^2\ g^{-1}$, while the average pore radius decreased from 1.66 nm to 1.105 nm, indicating the formation of a more refined and porous microstructure (Fig. S3a and b). X-ray photoelectron spectroscopy (XPS) was employed to analyze the surface chemical states and elemental environments of the LATP and LATP-J samples. Fig. 2f presents the spectra for Al 2 p, O 1s, P 2p, and Ti 2p. Consistent binding energies across both samples suggest that the chemical environments of these elements remain unchanged. The peaks at 465.3 and 459.2 eV in the Ti 2p spectrum correspond to Ti^{4+} in LATP. Interestingly, only Ti^{4+} signals appeared in LATP-J prepared by Joule heating, whereas the conventionally sintered LATP also exhibited Ti^{3+} signals, indicating partial reduction of Ti. Examination of the Ti 2p spectra of LATP-J samples sintered at different Joule heating temperatures (Fig. S4) revealed varying amounts of Ti^{3+} at 1000 °C, 1200 °C, and 1300 °C. This reduction of Ti^{4+} to Ti^{3+} compromises the stability of the active LATP phase, potentially degrading battery performance.[18,41]

The morphological and functional characterization of the PGPE@P-LATP10-J composite electrolyte

Enhancing the transmission efficiency of Li^+ within the inorganic phase and achieving uniform Li^+ deposition require not only structural design but also mechanical and thermal robustness.[42–44] To this end, a solution casting technique was adopted to fabricate LATP-based composite electrolyte membranes with improved overall integrity. Specifically, the LATP-J-based sols were cast into a PTFE mold and then heated to evaporate the solvent, forming a dense monolithic P-LATP-J membrane (Fig. 3a). A series of membranes were prepared by incorporating different amounts of LATP particles into the poly(vinylidene fluoride) (PVDF) matrix to determine the optimal LATP content. The tested compositions include 0 wt% LATP (pure PVDF), 5 wt% (denoted as P-LATP5), 7.5 wt% (P-LATP7.5), 10 wt% (P-LATP10), and 12.5 wt% (P-LATP12.5). XRD analysis (Fig. S4) revealed that the characteristic diffraction peaks of LATP remained unchanged across all samples, indicating that the presence of PVDF does not affect the crystalline structure of LATP. XRD measurements were first performed on samples with different LATP contents. The diffraction patterns showed no change in peak positions or intensities, indicating that the NASICON-type $LiTi_2(PO_4)_3$ structure is well preserved across all compositions (Fig. S5). Raman spectroscopy was subsequently employed to provide further structural insights. In all P-LATP membranes, the spectra consistently displayed the characteristic peaks at 949 cm^{-1} and 643 cm^{-1}. These peaks correspond to the asymmetric stretching vibrations of PO_4^{3-} groups and the vibrations of TiO_6 octahedra, respectively. The absence of additional or shifted peaks suggests that the structure of LATP remains intact and chemically stable in the polymer matrix (Fig. S6). FT-IR spectroscopy was also conducted to complement the structural analysis (Fig. S7). The spectra exhibited stable absorption bands at 1025 cm^{-1} and 612 cm^{-1}, which are attributed to the stretching and bending vibrations of PO_4^{3-} units. These bands remain unchanged across different LATP loadings, further confirming that no chemical interaction occurs between LATP and the PVDF polymer. Instead, the two components were physically mixed, maintaining their intrinsic structural features.

Subsequently, the thermal stability of electrolyte membranes with different LATP contents was evaluated. As shown in the TGA curves (Fig. S8), P-LATP10 and its Joule-heated counterpart P-LATP10-J exhibit superior thermal stability. This suggests that membrane performance does not increase linearly with LATP loading. Excess ceramic content tends to cause particle agglomeration due to the large specific surface area, which obstructs Li^+ transport and compromises thermal stability. Puncture tests on P-LATP10-J, P-LATP10, and PVDF were conducted to evaluate their resistance to localized mechanical stress (Fig. 3b). P-LATP10-J exhibited the highest puncture strength of 1.11 N, exceeding that of P-LATP10 (0.96 N) and PVDF (1.05 N), while its minimal displacement of 2.2 mm indicated superior stiffness. Based on its improved bulk mechanical performance, atomic force microscopy (AFM) was performed to further probe the nanoscale modulus. Fig. S9(a) and (b) show the surface morphologies and the corresponding elastic moduli of P-LATP10 and P-LATP10-J, measured as 1.2 and 2.37 GPa, respectively. These results confirm that P-LATP10-J maintains excellent mechanical robustness, which helps suppress deformation and lithium dendrite intrusion

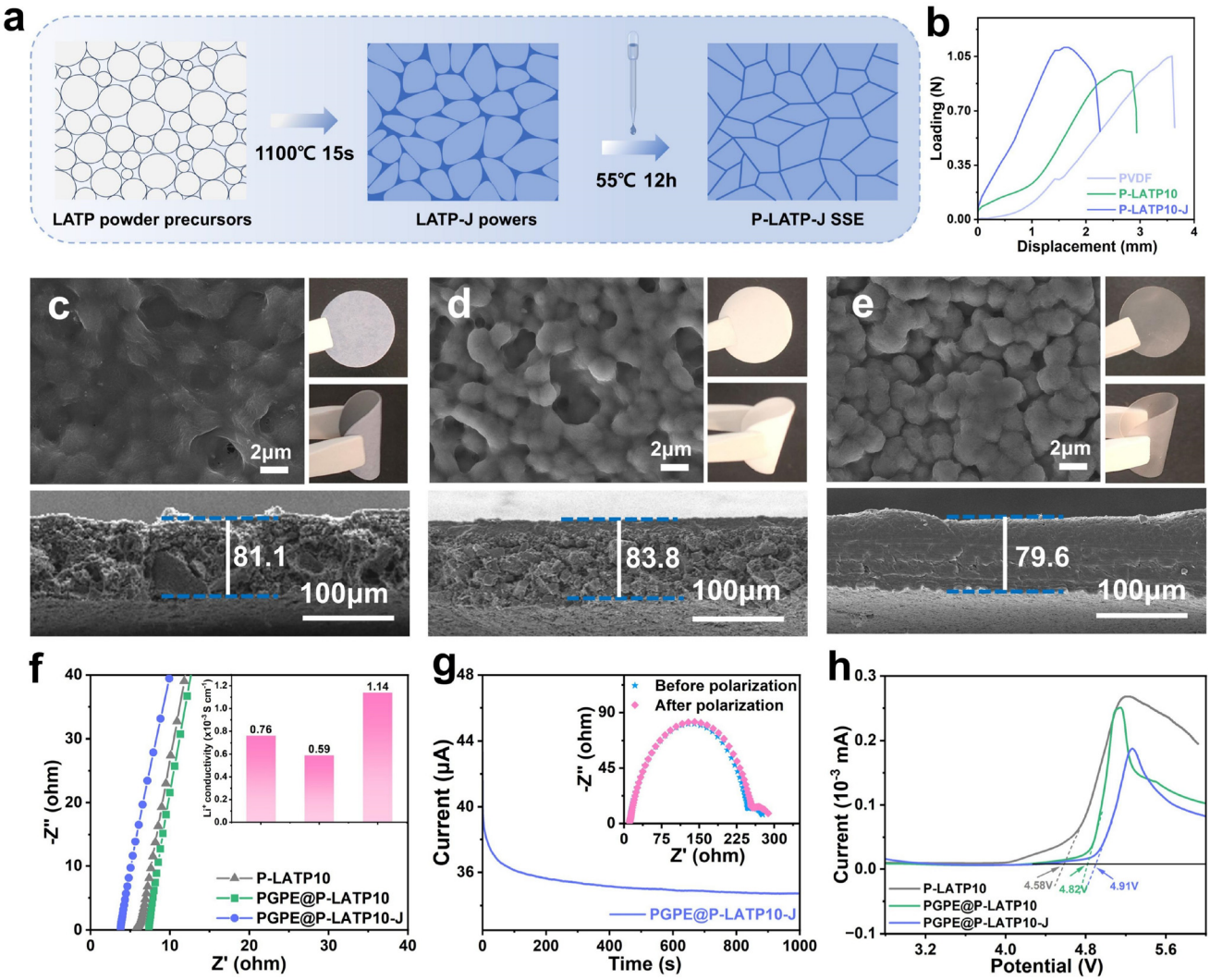

Fig. 3 Physical and chemical properties of PGPE@P-LATP-10-J. (a) The schematic diagram of the P-LATP-10-J layer preparation procedure. (b) The puncture strength of P-LATP-10-J, P-LATP10 and PVDF. (c–e) The surface and cross-section morphology of P-LATP10-J, P-LATP10 and PVDF, respectively. (f) The ionic conductivity of P-LATP10, PGPE@P-LATP10 and PGPE@P-LATP10-J at 30 °C. (g) Chronoamperometric curves of PGPE@P-LATP10-J (inset displays the EIS curves before and after polarization). (h) The linear sweep voltammetry (LSV) of P-LATP10, PGPE@P-LATP10 and PGPE@P-LATP10-J at a scan rate of 1 mV s^{-1}.

during cycling. The flame retardancy of PVDF, P-LATP10, and P-LATP10-J was evaluated *via* ignition tests. Fig. S10 shows that P-LATP10 and P-LATP10-J retain their original shape and size after 2 seconds of fire exposure, indicating high thermal stability and non-flammability, which confirms the crucial role of LATP-based membranes in improving battery safety and enabling LMBs to operate reliably under elevated temperatures.

Moreover, all three solution-cast films have uniformly smooth surfaces without cracks or holes, as confirmed by the inset images in the upper-right corners of Fig. 3c–e. Bending tests showed that each film maintains its integrity at bending angles greater than 90° without breaking or delamination, indicating good mechanical flexibility. Cross-sectional SEM images reveal that the films have similar thicknesses with values of 81.1 μm for P-LATP10-J, 83.8 μm for P-LATP10, and 79.6 μm for PVDF, demonstrating consistent membrane formation. Joule heating ultrafast sintering applied to P-LATP10-J results in fine grains with blurred grain boundaries, which suppress lithium volatilization and reduce grain boundary resistance, as shown in Fig. S11. In contrast, traditional solid-phase sintering used for P-LATP10 produces coarse grains with distinct grain boundaries, pores, and cracks that impede ion migration. In addition, elemental mapping confirmed the uniform distribution of aluminum, titanium, phosphorus, and oxygen in P-LATP10-J, ensuring structural integrity and continuous lithium-ion transport (Fig. S12).

To quantify the mechanical reinforcement provided by the PGPE interlayer, we measured its average Young's modulus. The resulting value of 1.2 MPa (Fig. S13) is three orders of

magnitude higher than the modulus of conventional liquid electrolytes (~1 kPa) and is sufficient to accommodate volume changes at the Li/LATP interface without fracture or loss of contact. The interfacial affinity and wettability between the PGPE precursor and the P-LATP10-J membrane were evaluated *via* contact angle measurements, as shown in Fig. S14. The contact angle of P-LATP10-J (17.37°) is smaller than that of the pristine PVDF membrane (28.46°) and the P-LATP10 membrane (20.06°), indicating enhanced wettability. This improvement in electrolyte affinity and liquid absorbability can be attributed to the presence of inorganic LATP-J ceramic particles, which increase surface roughness and contribute to the preservation of the interconnected pore structure, thereby enhancing the interfacial contact performance of P-LATP10-J. As illustrated in Fig. 3f, the incorporation of LATP10-J significantly enhances the ionic conductivity of the PGPE@P-LATP10-J membrane, which reaches 1.14 mS cm^{-1} at room temperature, higher than that of PGPE@P-LATP10 (0.57 mS cm^{-1}) and P-LATP10 (0.76 mS cm^{-1}). The Li^+ transference number (t_{Li^+}) of the PGPE@P-LATP10-J membrane in Fig. 3g reached 0.79. This is higher than that of PGPE@P-LATP10 (0.74, Fig. S15a) and P-LATP10 (0.45, Fig. S15b). The PGPE layer can form a fluorine-rich solid electrolyte interphase protective layer at the interface with the lithium metal anode, and its presence prevents the penetration of electrons, preventing them from reaching the inorganic lattice. By optimizing the diversity of ion transfer sites in the structure, the ionic mobility is increased, which is conducive to the coordination of ionic concentration and the reduction of side reactions. Meanwhile, the sintering process in the electric furnace was throughout carried out under an inert gas argon, which inhibited oxidation and component volatilization.[45,46] This enabled the P-LATP10-J membrane to form more stable Li^+ lanes, accelerating the migration of Li^+. Compared with P-LATP10 (4.58 V) and PGPE@P-LATP10 (4.82 V), PGPE@P-LATP10-J showed a wider electrochemical window of 4.91 V (Fig. 3h). The wide electrochemical window enables PGPE@P-LATP10-J to adapt to the high-pressure cathode and avoid electrolyte decomposition, and can effectively promote the migration of Li^+. This is due to the cross-linking of OFHDODA in the PGPE layer with the difluoromethyl chain, which has a strong electron-withdrawing effect and can reduce the electron density of the entire polymer network of the PGPE layer, improving the antioxidant capacity.[47]

Interfacial stability of the PGPE@P-LATP10-J composite electrolyte with lithium metal

The stability between the electrolyte and the Li anode was evaluated using the Li deposition/withdrawal capability in a Li–Li symmetric battery. Symmetric batteries with different electrolytes were assembled for testing (Fig. 4). The voltage–time graphs are shown in Fig. 4(a, c, and e), indicating that the polarization of all batteries increased with an increase in current density during the cycling. Under the condition of gradually increasing current, the polarization voltages of Li||P-LATP10||Li significantly increased, while those of Li||PGPE@P-LATP10||Li and Li||PGPE@P-LATP10-J||Li fluctuated less. In particular, when the current density increased to 1.0 mA cm^{-2}, the symmetric battery of Li||PGPE@P-LATP10-J||Li still cycled stably. However, the battery of Li||P-LATP10||Li became unstable at a current density of 0.5 mA cm^{-2}, and the polarization voltage of Li||PGPE@P-LATP10||Li weakened at a current density of 0.8 mA cm^{-2}. This confirmed that the high ionic conductivity of the PGPE layer and the excellent wettability of the P-LATP-J membrane could guide the uniform diffusion of lithium ions. More importantly, the rigid framework of the P-LATP10-J membrane and the flexible characteristics of the PGPE layer form a composite structure, which physically blocks the growth of dendrites while achieving a stable combination of the organic–inorganic interface, thereby restricting the dendrites within the PGPE layer and preventing them from diffusing into the inorganic electrolyte matrix. This multi-scale collaborative protection mechanism enables PGPE@P-LATP10-J to maintain stable lithium deposition/peeling behavior even under an extreme current (1.0 mA cm^{-2}). The stable current–voltage characteristics indicate that PGPE@P-LATP10-J has excellent electrode–electrolyte interface stability. Fig. 4(b, d, and f) show the time–voltage curves of the Li–Li symmetric battery at a current density of 0.5 mA cm^{-2}. After less than 300 hours of cycling, the polarization voltage began to fluctuate, indicating that the penetration of Li dendrites led to an internal short circuit. After introducing PGPE, Li||PGPE@P-LATP10||Li exhibited stable Li deposition/peeling behavior in the early stage and the polarization began to increase after 400 hours. As a comparison, Li||PGPE@P-LATP10-J||Li with LATP-J particles could stably cycle for over 1500 hours without any significant polarization change. Better cycling stability comes from the C–F bond energy in the PGPE layer, which effectively reduces the electron density of PGPE@P-LATP10-J and enhances its antioxidant capacity, avoiding changes in the LATP framework structure caused by redox reactions.[34] Meanwhile, the LATP-J particles are uniformly distributed throughout the P-LATP10-J membrane, maintaining a continuous porous structure and forming continuous Li^+ lanes, which is more conducive to the rapid passage of Li^+.

To directly visualize the inhibitory effect of PGPE@P-LATP10-J on lithium dendrite formation, the morphological evolution of lithium deposits was monitored using *in situ* optical microscopy under a deposition current of 2 mA cm^{-2}. As shown in Fig. 4g–i, the surface of Li||P-LATP10||Li was smooth before Li cycling, but after 10 minutes of cycling, obvious lithium dendrites could be observed on the surface of the lithium metal. In contrast, the lithium metal surfaces of Li||PGPE@P-LATP10||Li and Li||PGPE@P-LATP10-J||Li exhibited dendrite-free behavior throughout the electroplating process. From the trend of obvious lithium dendrite growth observed in the P-LATP10 layer after 10 minutes of charging, and the increase in the growth trend after 20 minutes, the P-LATP10 layer with added LE is not effective in inhibiting the growth of lithium dendrites. However, the introduced PGPE layer has high ionic conductivity and good compatibility with

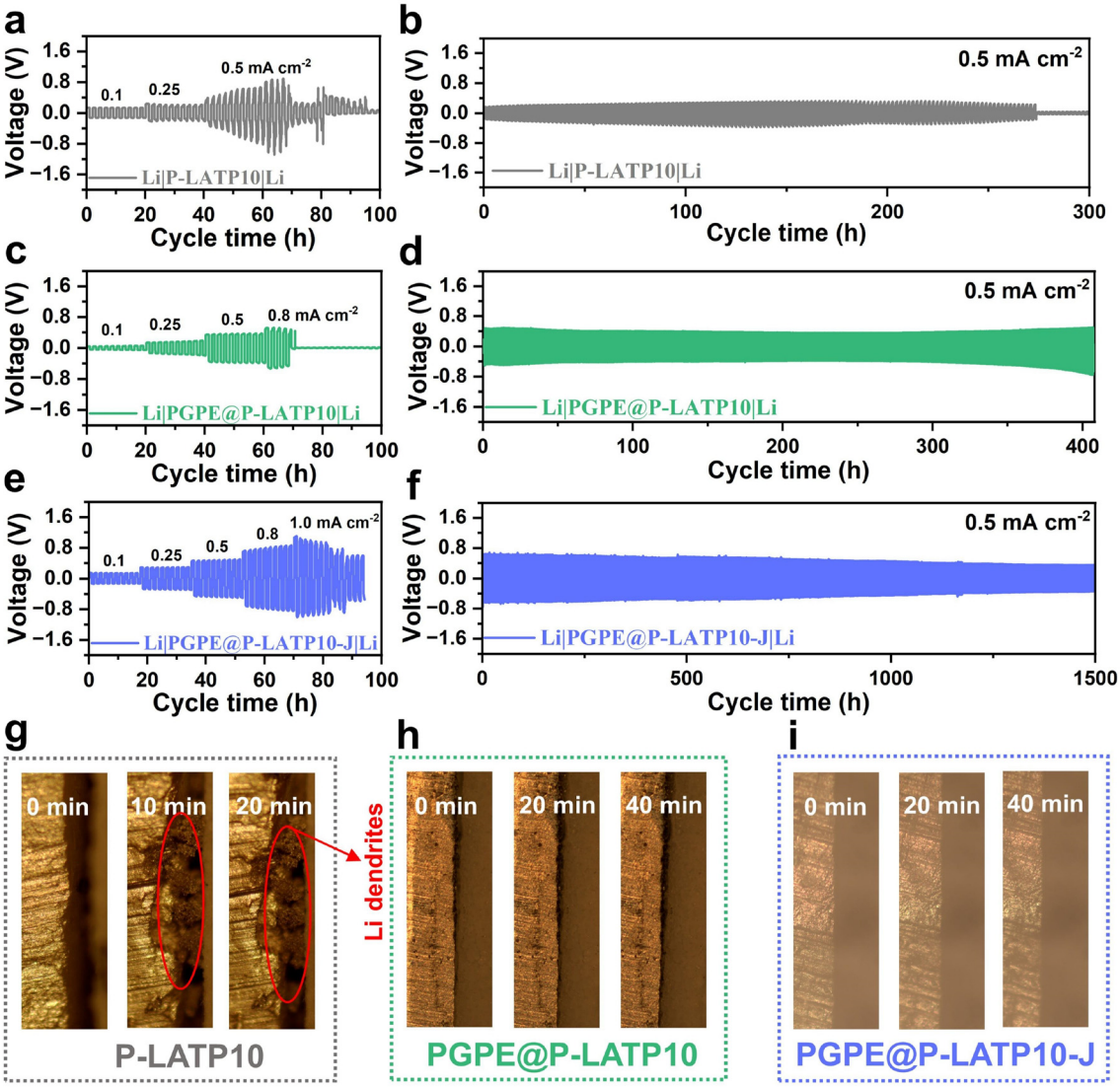

Fig. 4 Li metal compatibility in the interaction mechanism of the PGPE@P-LATP10-J composite layer. The Li plating/stripping cycling curves of Li symmetrical batteries with (a) P-LATP10, (c) PGPE@P-LATP10 and (e) PGPE@P-LATP10-J, respectively, at current densities of 0.1, 0.25, 0.5, 0.8, and 1 mA cm^{-2}. Long-term Li plating/stripping curves of (b) P-LATP10, (d) PGPE@P-LATP10 and (f) PGPE@P-LATP10-J at 0.5 mA cm^{-2}, respectively. *In situ* optical images of Li deposition in (g) P-LATP10, (h) PGPE@P-LATP10 and (i) PGPE@P-LATP10-J based Li electrodes, respectively, at a deposition current density of 2 mA cm^{-2}.

lithium metal, which can promote rapid and uniform Li^+ deposition/peeling. It suppresses interfacial side-reactions triggered by dendrite penetration and blocks their propagation into both the P-LATP10 layer and the P-LATP10-J membrane. By keeping lithium deposition uniform, the PGPE@P-LATP10-J composite layer prevents dendrite growth and enables stable long-term cycling in symmetric cells.

The electrochemical performance of the PGPE@P-LATP10-J composite electrolyte with various cathode materials

The electrochemical compatibility of PGPE@P-LATP10-J with different cathode materials was systematically evaluated. Coin cells using $LiCoO_2$ (LCO) as the cathode were assembled and tested at 30 °C within a voltage window of 3.0–4.2 V. As presented in Fig. 5a, the LCO||PGPE@P-LATP10-J||Li cell delivered specific capacities of 144.08, 141.07, 135.50, 124.02, and 106.96 mAh g^{-1} at current rates of 0.1C, 0.2C, 0.5C, 1C, and 2C, respectively. In comparison, the LCO||PGPE@P-LATP10||Li cell exhibited capacities of 145.33, 140.92, 122.77, 104.14, and 72.94 mAh g^{-1}, while the LCO||P-LATP10||Li configuration showed lower values of 138.78, 130.81, 117.64, 98.31, and 51.7 mAh g^{-1} under identical testing conditions. The PGPE@P-LATP10-J system exhibited superior rate capability, particularly under high-rate operation (2C), underscoring its improved ionic transport and interfacial stability. This enhancement is further corroborated by the charge–discharge profiles shown in Fig. 5b and Fig. S16a, b, where PGPE@P-LATP10-J displays higher voltage plateaus and

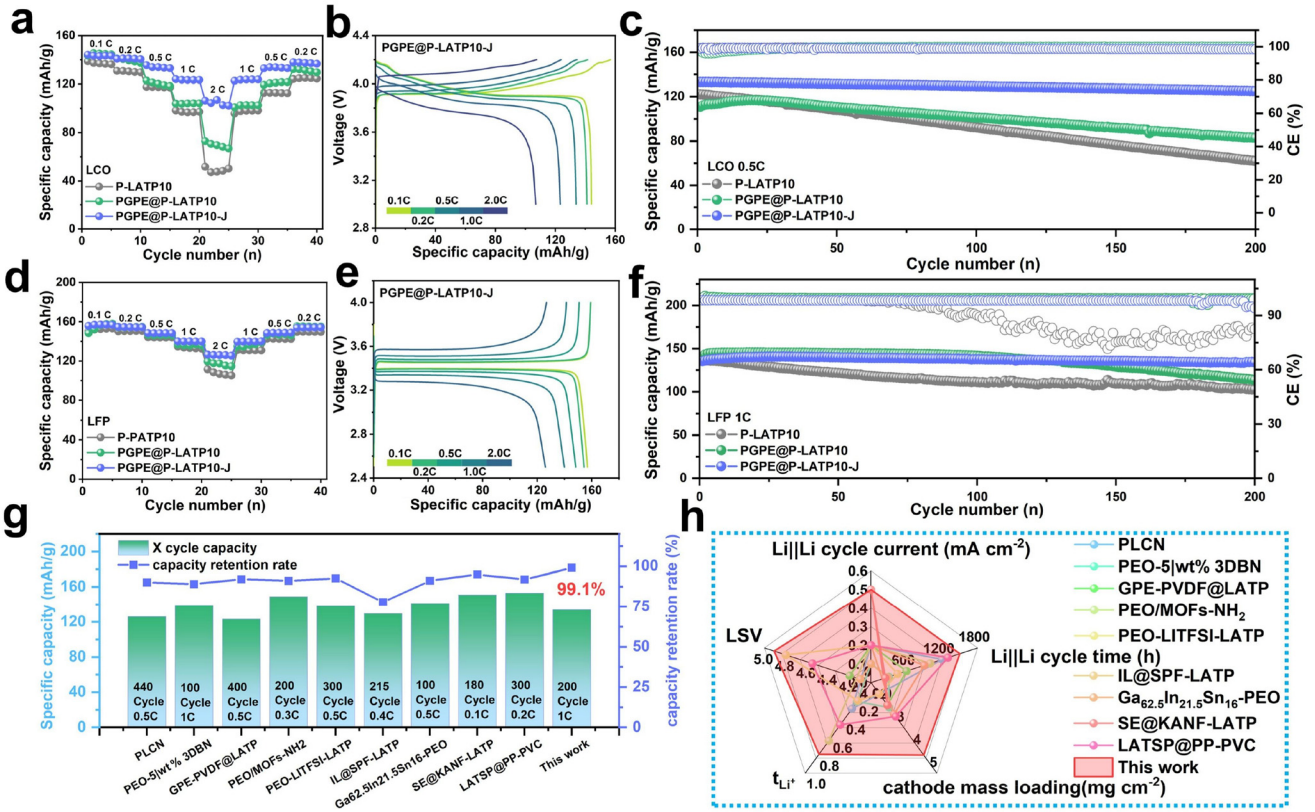

Fig. 5 Electrochemical performance of PGPE@P-LATP10-J. (a) Rate performance of P-LATP, PGPE@P-LATP10 and PGPE@P-LATP10-J based LCO||Li batteries. (b) Charge/discharge cycling curves of LCO||PGPE@P-LATP10-J||Li. (c) Cycling performance at 1C-rate of P-LATP, PGPE@P-LATP10 and PGPE@P-LATP10-J based LCO||Li batteries. (d) Rate performance of P-LATP, PGPE@P-LATP10 and PGPE@P-LATP10-J based LFP||Li batteries. (e) Charge/discharge cycling curves of LFP||PGPE@P-LATP10-J||Li. (f) Cycling performance at 1C-rate of P-LATP, PGPE@P-LATP10 and PGPE@P-LATP10-J based LFP||Li batteries. (g and h) Comparison of the electrochemical performances with other reported works.

reduced polarization compared to the other systems. These results confirm that the synergistic internal and external modification strategies effectively stabilize the electrode–electrolyte interface and enhance electrochemical kinetics. The corresponding long-term cycling performance is presented in Fig. 5c. The initial specific capacity of the LCO||PGPE@P-LATP10-J||Li battery is 133.3 mAh g^{-1}, which is lower than that of the LCO||PGPE@P |Li battery (135.41 mAh g^{-1}). However, after 200 cycles, the LCO||PGPE@P-LATP10-J||Li battery maintains a high specific capacity of 125.16 mAh g^{-1}, with a retention rate of 93.8%, clearly indicating that PGPE@P-LATP10-J has better compatibility with the high-voltage cathode. These cycled batteries were disassembled to investigate the interfacial reactions between LATP and the lithium anode. As shown in Fig. S17, the lithium anode of Li||PGPE@P-LATP10-J||LCO after cycling exhibits a smoother surface and fewer interfacial reaction products compared with those of Li||PGPE@P-LATP10||LCO and Li||P-LATP10||LCO. XRD analysis of the electrolyte membranes after cycling (Fig. S18) revealed the presence of pronounced lithiated LATP phases in P-LATP10, which confirms that interfacial side reactions remain severe. In PGPE@P-LATP10, the intensity of lithiated LATP peaks is reduced, indicating that the PGPE layer effectively suppresses Li/LATP side reactions. In contrast, PGPE@P-LATP10-J after cycling shows no detectable lithiated LATP peaks, suggesting that its composite structure maintains high interfacial stability.

To further validate its versatility, PGPE@P-LATP10-J was also evaluated in half-cell configurations employing LFP as the cathode. As depicted in Fig. 5d, the LFP||PGPE@P-LATP10-J||Li cell delivered specific discharge capacities of 157.1, 154.5, 148.4, 139.9, and 126.5 mAh g^{-1} at current densities of 0.1C, 0.2C, 0.5C, 1C, and 2C, respectively. In contrast, the corresponding capacities for LFP||PGPE@P-LATP10||Li were 154.6, 150.2, 141.6, 129.8, and 110.7 mAh g^{-1}, while those for LFP||P-LATP10||Li decreased to 148.2, 141.4, 131.0, 119.1, and 95.4 mAh g^{-1} under the same conditions. The superior performance of PGPE@P-LATP10-J, particularly at higher current rates, reflects its enhanced ionic conductivity and interfacial charge transfer efficiency. These findings confirm that the synergistic effects of internal structural optimization and external polymer infiltration impart the composite electrolyte with excellent rate capability and broad compatibility with cathode materials. The long-term cycling behavior of the assembled cells was further evaluated to assess their electrochemical durability. As shown in Fig. 5e and Fig. S19a, b, the

PGPE@P-LATP10-J-based cell exhibits highly stable and overlapping charge/discharge profiles, reflecting its efficient charge transport kinetics and excellent structural stability during repeated cycling. Fig. 5f presents the cycling performance at 1C over 200 cycles. The LFP||PGPE@P-LATP10-J||Li cell delivers an initial discharge capacity of 135.18 mAh g^{-1} and maintains 133.99 mAh g^{-1} after 200 cycles, corresponding to a capacity retention of 99.1%. In comparison, the LFP||PGPE@P-LATP10||Li and LFP||P-LATP10||Li cells exhibit initial capacities of 140.67 and 138.35 mAh g^{-1}, but decline to 113.53 and 102.46 mAh g^{-1}, with retention rates of only 80.7% and 74.05%, respectively. These results underscore the superior cycling stability of PGPE@P-LATP10-J, which benefits from both enhanced interfacial contact and suppressed structural degradation under long-term operation.

Electrochemical impedance spectroscopy (EIS) was performed on the variation of interfacial resistance of PGPE@P-LATP10-J, PGPE@P-LATP10 and P-LATP10 before and after the cycle with LFP as the cathode. As shown in Fig. S20a–c, the interfacial resistance (R_i) extracted from the half-cell EIS data before cycling and after the 200th cycle indicates that ion transport is significantly hindered in LFP||PGPE@P-LATP10||Li and LFP||P-LATP10||Li, with R_i increasing from 74.3 Ω cm^{-2}, 79.6 Ω cm^{-2} to 538 Ω cm^{-2}, 607 Ω cm^{-2} respectively. The applied equivalent circuit is depicted in Fig. S20d. In these two systems, heterogeneous charge carrier segregation at grain boundaries obstructs ion transport and leads to substantial interfacial resistance. In contrast, the R_i of LFP||PGPE@P-LATP10-J||Li increases from 57.9 Ω cm^{-2} to 197 Ω cm^{-2}, while the C–F bonds in the PGPE layer lower the electron density of PGPE@P-LATP10-J, thereby enhancing the antioxidant capacity of the inorganic layer and improving interfacial reaction kinetics. The increase in impedance observed for P-LATP10 is attributed to adverse interface side reactions caused by compression of the lithium metal anode on P-LATP, which induces local stress and ultimately disrupts the electrode–electrolyte interface stability. Compared to PGPE@P-LATP10-J, which benefits from both internal and external modifications, P-LATP10 lacks thermodynamic stability and sufficient ionic conductivity, leading to electrolyte decomposition during cycling, significant interface impedance growth, and hindered lithium-ion transport. When compared to recently reported solid-state batteries based on LATP and composite electrolytes (Fig. 5g–h and Table S1), the newly synthesized PGPE@P-LATP10-J composite electrolyte demonstrates significant advantages in overall performance, especially in efficient Li^+ transport, robust cycling stability, high-temperature tolerance, and high-voltage stability.

In situ characterization of the interaction mechanism of the PGPE@P-LATP10-J composite electrolyte

To monitor gas evolution during the charge–discharge process and clarify the role of the PGPE layer in regulating interfacial chemical reactions, an *in situ* differential electrochemical mass spectrometry (DEMS) system coupled with electrochemical testing was employed. Real-time analysis of gas generation was conducted for cells within the voltage range of 2.5–4.0 V. As shown in Fig. S21 and Fig. 6a and b, the LFP||P-LATP10||Li cell exhibits a pronounced CO_2 signal (m/z = 44) during the first 2 hours of charging, indicating that irreversible side reactions occur at the interface between the inorganic solid-state electrolyte (P-LATP10) and the lithium metal anode. These reactions lead to oxidative decomposition of electrolyte components, such as carbonate solvents and lithium salts.[48] The continuous CO_2 evolution accelerates electrolyte consumption and increases internal cell pressure, ultimately compromising the cycle life and safety of the solid-state battery. In contrast, no detectable CO_2 signals were observed in the LFP||PGPE@P-LATP10||Li and LFP||PGPE@P-LATP10-J||Li cells throughout the full charge–discharge process, demonstrating that the PGPE layer effectively suppresses interfacial decomposition *via* physical isolation and chemical passivation, thus stabilizing the lithium metal interface.

The dynamic interfacial evolution of the PGPE layer during the charge–discharge process was further investigated using *in situ* Fourier-transform infrared spectroscopy (FTIR), which enabled real-time monitoring of the LFP||PGPE@P-LATP10-J||Li system. As presented in Fig. 6c and d and Fig. S22, the infrared characteristic peak intensities corresponding to C–F bonds (850 cm^{-1}) and C–O–C bonds (1200 cm^{-1}) in the PGPE layer exhibit highly reversible variations with the change in voltage. During the charging process, the vibration intensities of both C–F and C–O–C bonds increase significantly, whereas a gradual return to the initial state is observed upon discharging. This reversible spectral response is associated with the dynamic coordination of polar functional groups (C–F and C–O–C) with lithium ions.[49,50] As lithium ions migrate from the cathode into the electrolyte during charging, these polar groups electrostatically adsorb Li^+, inducing a change in molecular vibration modes and leading to increased peak intensities. During discharging, the desorption of lithium ions results in the restoration of the original molecular configuration, accompanied by a reduction in peak intensity. Such a directional Li^+ coordination-release behavior facilitates uniform ion transport and mitigates the loss of active lithium at the interface. In contrast, the P-LATP10 system without the PGPE layer shows irregular fluctuations in infrared peak intensities throughout cycling. These observations suggest that the absence of a functional interfacial layer limits the ability to regulate lithium-ion transport, resulting in non-uniform lithium deposition and intensified parasitic reactions.

In situ Raman spectroscopy was further used to explore the correlation between lithium-ion transport and the structural evolution of the PGPE@P-LATP10-J composite electrolyte during electrochemical cycling. As shown in Fig. 6e and f and Fig. S23, the Raman peaks corresponding to the LATP ceramic phase at 135.3 cm^{-1} (Ti–O vibration), 343.1 cm^{-1} (symmetric stretching of PO_4^{3-}), and 998.6 cm^{-1} (asymmetric stretching of PO_4^{3-}) gradually decrease in intensity when the voltage increases to 4.0 V during charging, and then gradually recover to the initial levels during discharging. This regular and reversible variation in peak intensities reflects the structural

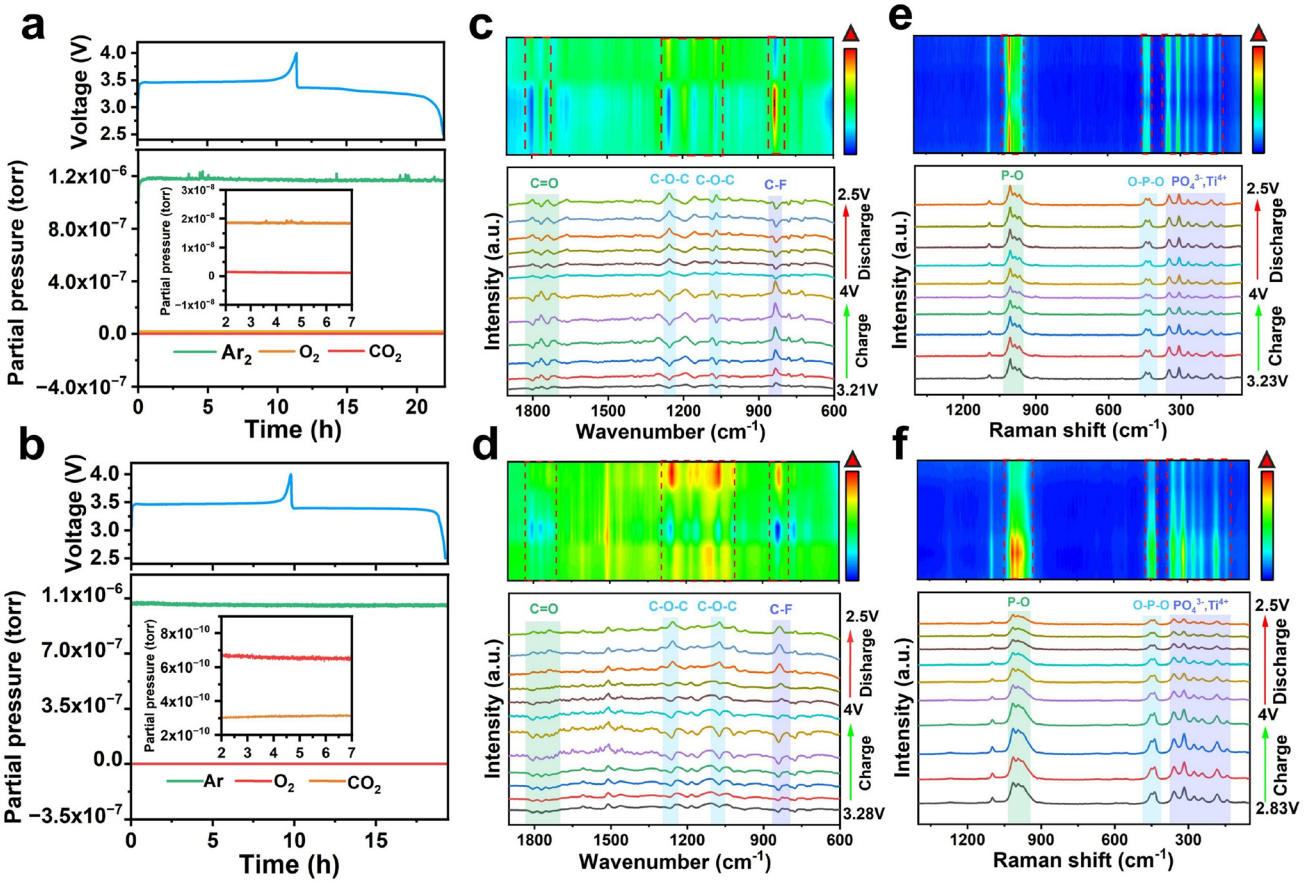

Fig. 6 *In situ* characterization of the interaction mechanism of the PGPE@P-LATP10-J composite layer. Voltage profile and the corresponding *in situ* DEMS results of various mass signals of (a) PGPE@P-LATP10-J and (b) PGPE@P-LATP10, respectively. *In situ* FT-IR spectra and the corresponding contour mapping of (c) PGPE@P-LATP10-J and (d) PGPE@P-LATP10, respectively. *In situ* Raman spectra and the corresponding contour mapping of (e) PGPE@P-LATP10-J and (f) PGPE@P-LATP10, respectively.

response of the ceramic framework to lithium-ion migration. According to previous studies by Emery[51] *et al.*, lithium ions move through triangular oxygen planes formed between Ti/AlO_6 octahedra and PO_4 tetrahedra, which induces stretching and local deformation of the Ti/AlO_6 units. During charging, the migration of lithium ions from the cathode to the anode alters the local environment of these structural units, leading to a temporary weakening of the corresponding vibrational modes. During discharging, the return of lithium ions restores the original configuration, resulting in the recovery of peak intensity. The observed reversibility in Raman signals indicates that the LATP-J layer prepared by the Joule-heating process maintains a pure phase structure and dense morphology. These features provide a continuous and low-impedance pathway for lithium-ion transport, enhancing the overall migration kinetics. In contrast, the P-LATP10 and PGPE@P-LATP10 membranes do not show consistent changes in Raman peak intensities during cycling. This irregularity suggests that the discontinuities and defects in their microstructures hinder ion transport, increase interfacial resistance, and limit the structural adaptability of the electrolyte during operation.

To reveal in depth the potential stabilizing mechanism at the Li/LATP interface and clarify the regulatory role of PGPE on interfacial performance from the perspectives of electronic structure and charge transfer, density functional theory (DFT) calculations were employed for a systematic analysis. Two comparative interface models were constructed to explore the intervention effect of PGPE. One model represents direct contact of Li/LATP without an intermediate layer (Fig. 7a), while the other represents a Li/PGPE/LATP composite interface model incorporating a PGPE intermediate layer (Fig. 7b). The projected density of states (PDOS) was analyzed to characterize the differences in electronic behavior between the two interfaces. As observed in Fig. 7c, the Li/LATP interface exhibits obvious conduction band characteristics, which provide free transmission channels for electrons, thereby facilitating electron injection and subsequent interfacial side reactions. After the introduction of PGPE, the PDOS of the interface shifts toward the Fermi level, which narrows the band gap and theoretically enhances electron excitation and transport (Fig. 7d). The regulatory effect of PGPE on interfacial charge transfer is examined through differential charge density simulations (Fig. 7e and f), where yellow represents charge accumulation

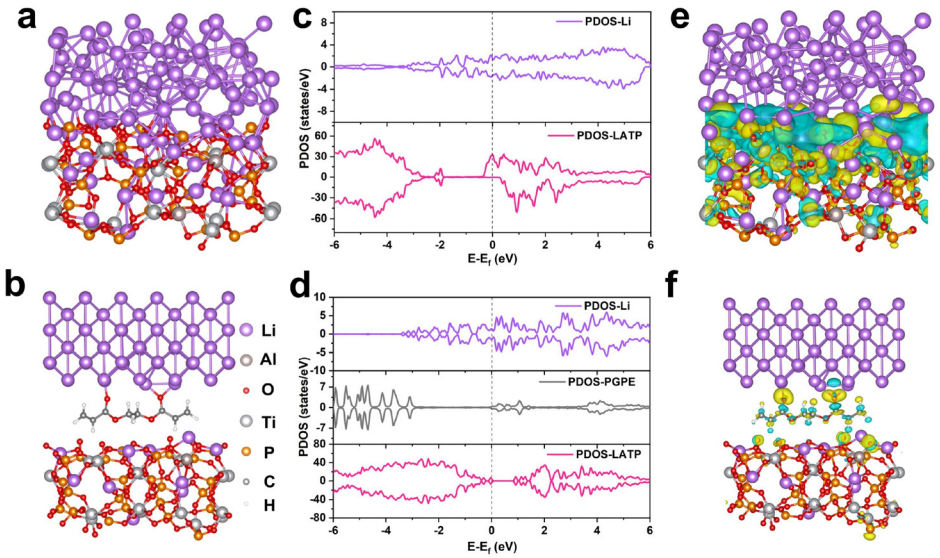

Fig. 7 (a and b) The interface model structures of Li/LATP and Li/PGPE/LATP, respectively. (c and d) The PDOS of Li/LATP and Li/PGPE/LATP, respectively. (e and f) The charge density difference of Li/LATP and Li/PGPE/LATP, respectively.

and blue represents charge depletion. The results reveal that the Li/LATP interface exhibits obvious charge transfer accompanied by an observably heterogeneous charge distribution, thereby reducing interfacial stability. In contrast, the introduction of PGPE significantly weakens interfacial charge transfer and renders the charge distribution more uniform, indicating that PGPE improves interface stability by suppressing interfacial charge transfer. The above results indicate that PGPE stabilizes the Li/LATP interface by simultaneously inhibiting electron injection, lowering electronic conductivity, and weakening interfacial charge transfer.

3. Conclusion

In summary, a novel composite PGPE@P-LATP-J solid-state electrolyte system was successfully synthesized by integrating a densified LATP ceramic and an *in situ* crosslinked PEGDA-based gel polymer layer. The densified LATP prepared *via* ultra-fast Joule heating exhibited reduced grain boundary resistance and enhanced lithium-ion conductivity. The introduction of the PEGDA-based interfacial layer further improved compatibility with lithium metal, effectively suppressing interfacial side reactions and enabling uniform Li^+ deposition and stripping. The resulting PGPE@P-LATP-J composite electrolyte exhibited a wide electrochemical window (4.91 V), high ionic conductivity (1.14×10^{-3} S cm^{-1}), and a high lithium-ion transference number (0.79), contributing to excellent electrochemical performance. The modified electrolyte enables solid-state LFP||Li cells to retain 99.1% of their initial capacity after 200 cycles and ensures long-term stability of Li||Li symmetric cells for more than 1500 hours. Furthermore, *in situ* characterization and theoretical calculations further elucidated the structural evolution and interfacial stabilization mechanisms of the composite electrolyte during cycling. This work provides a feasible and scalable pathway to overcome the intrinsic interface challenges of LATP-based electrolyte systems and offers valuable guidance for the design of high-performance solid-state lithium batteries.

Author contributions

H. G. and Q. L. conceived and designed the experiment and participated in the writing and revision of the paper. M. Y. conducted the electrochemical tests, analyzed the data, and wrote the manuscript. K. Z. and G. F. Z. carried out the TEM measurements. L. Y. and Q. X. H. synthesized the samples and characterized the LATP structure. X. L. L. performed the DFT simulation. S. Y. Y. conducted the FT-IR measurements. All authors have read and approved the final paper.

Conflicts of interest

The authors declare that they have no competing interests.

Data availability

The data that support the findings of this study are available in the paper and its supplementary information (SI). The SI incorporates the experimental data, XRD patterns, XPS spectra, BET test, and electrochemical performance of different samples. See DOI: https://doi.org/10.1039/d5eb00166h.

Acknowledgements

The authors would like to acknowledge financial support provided by the National Natural Science Foundation of China (52372232, 52303283, 52462037), the Major Science and Technology Projects of Yunnan Province (202302AB080019-3), the National Natural Science Foundation of Yunnan Province (202301AS070040, 202401AU070201), the Major Science and Technology Projects of Yunnan Province (202403AA080019), and Yunnan University Professional Degree Graduate Practice and Innovation Fund Project (ZC-242410156). The authors acknowledge the Advanced Analysis and Measurement Center of Yunnan University for the sample testing service and the Electron Microscopy Center of Yunnan University for the support of this work. The authors would like to thank Shiyanjia Lab (https://www.shiyanjia.com) for the AFM test.

References

1 K. Lin, X.-F. Xu, X.-Y. Qin, M. Liu, L. Zhao, Z.-J. Yang, Q. Liu, Y.-H. Ye, G.-H. Chen, F.-Y. Kang and B.-H. Li, *Nano–Micro Lett.*, 2022, **14**, 149.
2 J. Xie and Y.-C. Lu, *Nat. Commun.*, 2020, **11**, 2499.
3 G.-X. Lu, J. Nai, D.-Y. Luan, X.-Y. Tao and X.-W. Lou, *Sci. Adv.*, 2023, **9**, eadf1550.
4 W.-B. Zhang, P. Sayavong, X. Xiao, S. T. Oyakhire, S. B. Shuchi, R. A. Vila, D. T. Boyle, S. C. Kim, M. S. Kim, S. E. Holmes, Y. S. Ye, D. L. Li, S. F. Bent and Y. Cui, *Nature*, 2024, **626**, 306–312.
5 J.-G. Zhang, W. Xu, J. Xiao, X. Cao and J. Liu, *Chem. Rev.*, 2020, **120**, 13312–13348.
6 M.-J. Li, R. P. Hicks, Z.-F. Chen, C. Luo, J.-C. Guo, C.-S. Wang and Y.-H. Xu, *Chem. Rev.*, 2023, **123**, 1712–1773.
7 F. Ding, W. Xu, X.-L. Chen, J. Zhang, M. H. Engelhard, Y.-H. Zhang, B. R. Johnson, J. V. Crum, T. A. Blake, X.-J. Liu and J.-G. Zhang, *J. Electrochem. Soc.*, 2013, **160**, A1894–A1901.
8 Z.-F. Sun, Q.-Z. Yin, H.-Y. Chen, M. Li, S.-H. Zhou, S.-F. Wen, J.-H. Pan, Q.-Z. Zheng, B. Jiang, H.-D. Liu, K. Kim, J. Li, X. Han, Y.-B. He, L. Zhang, M.-C. Li and Q.-B. Zhang, *Interdiscip. Mater.*, 2023, **2**, 635–663.
9 J. Li, M.-S. Zhou, H.-H. Wu, L.-F. Wang, J. Zhang, N.-T. Wu, K.-M. Pan, G.-L. Liu, Y.-G. Zhang, J.-J. Han, X.-M. Liu, X. Chen, J.-Y. Wan and Q.-B. Zhang, *Adv. Energy Mater.*, 2024, **14**, 2304480.
10 P. Knauth, *Solid State Ionics*, 2009, **180**, 911–916.
11 C. Wang, Q. Sun, Y. Liu, Y. Zhao, X. Li, X. Lin, M. N. Banis, M. Li, W. Li and K. R. Adair, *Nano Energy*, 2018, **48**, 35–43.
12 S. Stramare, V. Thangadurai and W. Weppner, *ChemInform*, 2003, **34**, 3974–3990.
13 W. Xiao, J.-Y. Wang, L. Fan, J. Zhang and X. Li, *Energy Storage Mater.*, 2019, **19**, 379–400.
14 K. Yang, L.-K. Chen, J.-B. Ma, Y.-B. He and F.-Y. Kang, *InfoMat*, 2021, **3**, 1195–1217.
15 Z.-Y. Ning, G.-C. Li, D. L. R. Melvin, Y. Chen, J.-F. Bu, D. Spencer-Jolly, J.-L. Liu, B.-K. Hu, X.-W. Gao, J. Perera, C. Gong, S. D. D. Pu, S. M. Zhang, B.-Y. Liu, G. O. Hartley, A. J. Bodey, R. I. Todd, P. S. Grant, D. E. J. Armstrong, T. J. Marrow, C. W. Monroe and P. G. Bruce, *Nature*, 2023, **618**, 287–283.
16 W.-R. Zhang, V. Koverga, S.-F. Liu, J.-G. Zhou, J. Wang, P.-X. Bai, S. Tan, N. K. Dandu, Z.-Y. Wang, F. Chen, J.-L. Xia, H.-L. Wan, X.-Y. Zhang, H.-C. Yang, B.-L. Lucht, A.-M. Li, X.-Q. Yang, E.-Y. Hu, S. R. Raghavan, A. T. Ngo and C.-S. Wang, *Nat. Energy*, 2024, **9**, 386–400.
17 G.-J. Lu, M.-H. Li, P. Chen, W.-K. Zheng, Z.-G. Yang, R.-H. Wang and C.-H. Xu, *Energy Environ. Sci.*, 2023, **16**, 1049–1061.
18 J. A. Dawson, P. Canepa, T. Famprikis, C. Masquelier and M. S. Islam, *J. Am. Chem. Soc.*, 2018, **140**, 362–368.
19 L. Luo, Z. Sun, Y. You, X. Han, C. Lan, S. Pei, P. Su, Z. Zhang, Y. Li and S. Xu, *ACS Nano*, 2024, **18**, 2917–2927.
20 X. Zhu, J. Wu and J. Lu, *Adv. Funct. Mater.*, 2024, **34**, 2409547.
21 X.-G. Hao, Q. Zhao, S.-M. Su, S.-Q. Zhang, J.-B. Ma, L. Shen, Q.-P. Yu, L. Zhao, Y. Liu, F.-Y. Kang and Y.-B. He, *Adv. Energy Mater.*, 2019, **9**, 1901604.
22 J.-H. Yu, Q. Liu, X. Hu, S.-W. Wang, J.-R. Wu, B. Liang, C.-P. Han, F.-Y. Kang and B.-H. Li, *Energy Storage Mater.*, 2022, **46**, 68–75.
23 Q. Cheng, A. Li, N. Li, S. Li, A. Zangiabadi, T.-D. Li, W. Huang, A.-C. Li, T. Jin and Q. Song, *Joule*, 2019, **3**, 1510–1522.
24 J.-Y. Liang, X.-X. Zeng, X.-D. Zhang, T.-T. Zuo, M. Yan, Y.-X. Yin, J.-L. Shi, X.-W. Wu, Y.-G. Guo and L.-J. Wan, *J. Am. Chem. Soc.*, 2019, **141**, 9165–9169.
25 D. Yang, Y. Yang, Y. Sun and T. Zhang, *Adv. Funct. Mater.*, 2024, **35**, 2420202.
26 Y. G. Cho, C. Hwang, D. S. Cheong, Y. S. Kim and H. K. Song, *Adv. Mater.*, 2019, **31**, 1804909.
27 Q. Liu, L. Yang, Z.-Y. Mei, Q. An, K. Zeng, W.-J. Huang, S.-M. Wang, Y.-J. Sun and H. Guo, *Energy Environ. Sci.*, 2024, **17**, 780–790.
28 Q. Liu, Q. An, K. Zeng, M. Yang, H.-Y. Zhu, X.-L. Liang, G.-Q. Zhao, M.-J. Sun, Y.-C. Zha, L. Yang, L.-Y. Duan, G.-F. Zhao, Y.-J. Sun and H. Guo, *Energy Environ. Sci.*, 2025, **18**, 4934–4948.
29 Y.-Y. Cui, X.-M. Liang, J.-C. Chai, Z.-L. Cui, Q.-L. Wang, W.-S. He, X.-C. Liu, Z.-H. Liu, G.-L. Cui and J.-W. Feng, *Adv. Sci.*, 2017, **4**, 1700174.
30 Q. Zhao, X.-T. Liu, S. Stalin, K. Khan and L. A. Archer, *Nat. Energy*, 2019, **4**, 365–373.
31 H. He, Y. Wang, M. Li, J.-Y. Qiu, Y.-H. Wen and J.-H. Chen, *Chem. Eng. J.*, 2023, **467**, 143311.
32 H. Duan, Y.-X. Yin, X.-X. Zeng, J.-Y. Li, J.-L. Shi, Y. Shi, R. Wen, Y.-G. Guo and L.-J. Wan, *Energy Storage Mater.*, 2018, **10**, 85–91.
33 H. Zhang, X. Judez, A. Santiago, M. Martinez-Ibañez, M. A. Muñoz-Márquez, J. Carrasco, C. M. Li, G. G. Eshetu and M. Armand, *Adv. Energy Mater.*, 2019, **9**, 1900763.

34 K. Zeng, Q. Liu, H. Ma, G.-F. Zhao, Q. An, C.-H. Zhang, Y.-X. Yang, M.-J. Sun, Q.-J. Xu, L.-Y. Duan and H. Guo, *Energy Storage Mater.*, 2024, **70**, 103564.
35 J. Fu, *Solid State Ionics*, 1997, **104**, 191–194.
36 X.-X. Xu, Z.-Y. Wen, X.-L. Yang, J.-C. Zhang and Z.-H. Gu, *Solid State Ionics*, 2006, **177**, 2611–2615.
37 J.-F. Wu and X. Guo, *Phys. Chem. Chem. Phys.*, 2017, **19**, 5880–5887.
38 J. Zhu, J. Zhao, Y. Xiang, M. Lin, H. Wang, B. Zheng, H. He, Q. Wu, J.-Y. Huang and Y. Yang, *Chem. Mater.*, 2020, **32**, 4998–5008.
39 L.-J. Dai, J. Wang, Z.-X. Shi, L.-N. Yu and J. Shi, *Ceram. Int.*, 2021, **47**, 11662–11667.
40 B. Yang, X.-H. Li, H.-J. Guo, Z.-X. Wang and W. Xiao, *J. Alloys Compd.*, 2015, **643**, 181–185.
41 B. He, Y. Zhong, Z. Yan, T. Liu, X. Liu, Y. Du, Y. Yang, L. Yang, R. Zhang and Y. Su, *Adv. Funct. Mater.*, 2025, **35**, 2416779.
42 X. Zhan, M. Li, X.-L. Zhao, Y.-N. Wang, S. Li, W.-W. Wang, J.-D. Lin, Z.-A. Nan, J.-W. Yan, Z.-F. Sun, H.-D. Liu, F. Wang, J.-Y. Wan, J.-J. Liu, Q.-B. Zhang and L. Zhang, *Nat. Commun.*, 2024, **15**, 1056.
43 S. Wen, Z. Sun, X. Wu, S. Zhou, Q. Yin, H. Chen, J. Pan, Z. Zhang, Z. Zhuang and J. Wan, *Adv. Funct. Mater.*, 2025, 2422147.
44 X. Han, L.-H. Gu, Z.-F. Sun, M.-F. Chen, Y.-G. Zhang, L.-S. Luo, M. Xu, S.-Y. Chen, H.-D. Liu, J.-Y. Wan, Y.-B. He, J.-Z. Chen and Q.-B. Zhang, *Energy Environ. Sci.*, 2023, **16**, 5395–5408.
45 R. Wang, Q. Dong, C. Wang, M. Hong, J. Gao, H. Xie, M. Guo, W. Ping, X. Wang and S. He, *Adv. Mater.*, 2021, **33**, 2100726.
46 M. Hong, Q. Dong, H. Xie, X.-Z. Wang, A. H. Brozena, J.-L. Gao, C. W. C. J. Chen, J.-C. Rao and L.-B. Hu, *Mater. Today*, 2021, **42**, 41–48.
47 M.-C. Long, T. Wang, P.-H. Duan, Y. Gao, X.-L. Wang, G. Wu and Y.-Z. Wang, *J. Energy Chem.*, 2022, **65**, 9–18.
48 S. Wang, P. Xiong, J. Zhang and G. Wang, *Energy Storage Mater.*, 2020, **29**, 310–331.
49 C. Wang, Z. Guo, S. Zhang, G. Chen, S. Dong and G. Cui, *Energy Storage Mater.*, 2021, **43**, 221–228.
50 G. Song, Z.-L. Yi, F.-Y. Su, L.-J. Xie, Z.-B. Wang, X.-X. Wei, G.-N. Xu and C.-M. Chen, *ACS Energy Lett.*, 2023, **8**, 1336–1343.
51 J. l. Emery, T. Šalkus, A. Abramova, M. Barré and A. F. Orliukas, *J. Phys. Chem. C*, 2016, **120**, 26173–26186.